communications physics

A Nature Portfolio journal

Article

https://doi.org/10.1038/s42005-025-02190-2

Large bandgap observed on the surfaces of $EuZn_2As_2$ single crystals

Dejia Kong[1], Siavash Karbasizadeh[2], Ganesh Narasimha[3], Paras Regmi[2], Chenggang Tao[4], Sai Mu[2], Rama Vasudevan[3], Ian Harrison[1], Rongying Jin[2] ✉ & Zheng Gai[3] ✉

EuM_2As_2 (M = Zn, Cd, In, Sn etc.) is an excellent material system for studying magnetism-tuned topological properties. However, discrepancies exist between experimental data and theoretical calculations regarding the bulk and surface bandgaps. In this work, cleaved $EuZn_2As_2$ crystals are studied using scanning tunneling microscopy/spectroscopy and density functional theory calculations. Triangular-shaped defect-induced modifications in the local density of states help distinguish between Eu-terminated and AsZn-terminated surfaces. While large bandgaps (~1.5 eV at 77 K) are observed on both pristine surfaces, the bandgap size is found to be highly sensitive to local heterogeneity, tending to decrease. By combining experimental observations with theoretical simulations, we conclude that the reduced bandgap in heterogeneous regions arises from Zn vacancies and/or substitution by As atoms, both impacting greater in the Eu surface electronic properties than those in the AsZn surface. This demonstrates the intimate relationship between the electronic structure and magnetism in $EuZn_2As_2$.

In the topological physics community, topological materials with magnetism are extremely attractive, as they exhibit unique physical properties arising from the interplay between their topological electronic structures and magnetic ordering. In particular, their ability to support chiral electron channels with robust and controllable spin-dependent transport properties makes them highly promising for potential applications in spintronics and quantum computing[1,2]. In the search for magnetic topological materials, EuM_2As_2 (M = Zn, Cd, In, Sn, etc.) compounds have received extensive attention. The excitement was initially generated by intensive experimental and theoretical investigations on $EuCd_2As_2$, which suggested that its electronic structure is topologically protected because of its combined crystallographic and magnetic structures[3,4]. In particular, angle-resolved photoemission spectroscopy (ARPES) measurements indicate the topological phase transition from the Weyl state with a single pair of Weyl points above the Eu ordering temperature T_N ~ 9 K to the Dirac state below T_N[3,5]. Eu moment direction in $EuIn_2As_2$ determines the formation of either the axion-insulating state or topological-insulating state[6,7]. Eu-based compounds are thus considered an ideal platform for studying the relationship between electronic topology and magnetism, with switchable topological states solely controlled by magnetism. Naturally, the electronic structure of such a system depends strongly on the magnetic configurations for both bulk and surface[3–6,8,9].

However, none of the EuM_2As_2 family members has been studied thoroughly. For example, both band calculations and experiments suggest $EuCd_2As_2$ is a topological semimetal[3,5]. There is accumulating evidence for the deviation of the semi-metallic behavior for $EuCd_2As_2$ with a low carrier density[10–12]. The semiconducting nature with the bandgap around 0.77 eV has been observed for both bulk[10] and surface[13]. Earlier observation of the metallic transport in $EuCd_2As_2$ could result from band bending at the surface[11]. To investigate the electronic properties at the surface, scanning tunneling microscopy/spectroscopy (STM/S) is an ideal probe, which offers the direct measurement of the local density of states (LDOS) at the atomic level. STM experiments conducted on $EuIn_2As_2$ yielded a partial Eu-terminated surface after cleavage at room temperature[14] and 20 K[15]. However, such partial Eu termination was not observed in $EuCd_2As_2$[13]. Given that the crystal structure of $EuCd_2As_2$ (P-3m1) is slightly different from $EuIn_2As_2$ ($P6_3/mmc$), the comparison of the surface termination between them may not be straightforward, however.

Among existing EuM_2As_2 compounds, $EuZn_2As_2$ forms the same structure as $EuCd_2As_2$[16]. Due to closer packing, Eu in $EuZn_2As_2$ orders antiferromagnetically at T_N ~ 19 K[16,17], double that for $EuCd_2As_2$[3,4]. Above T_N, magnetic fluctuation persists to ~200 K[17], below which the anomalous Hall effect is observed. Since magnetism plays a crucial role in the topological properties of $EuCd_2As_2$ as seen by ARPES[3,5], one would expect

[1]Department of Chemistry, University of Virginia, Charlottesville, VA, 22903, USA. [2]SmartState Center for Experimental Nanoscale Physics, Department of Physics and Astronomy, University of South Carolina, Columbia, SC, 29208, USA. [3]Center for Nanophase Materials and Sciences, Oak Ridge National Laboratory, Oak Ridge, TN, 37831, USA. [4]Institute for Critical Technology and Applied Science, Department of Materials Science and Engineering, Virginia Tech, Blacksburg, VA, 24061, USA. ✉e-mail: rjin@mailbox.sc.edu; gaiz@ornl.gov

$EuZn_2As_2$ to behave similarly in its electronic properties. Therefore, conducting extensive experiments both above and below T_N in $EuZn_2As_2$ is equally important for a comprehensive understanding of the interplay between electronic topology and magnetism. At present, the surface-state properties of $EuZn_2As_2$ are unknown, to the best of our knowledge. Especially, is there evidence for nontrivial electronic topology as seen in $EuCd_2As_2$ by ARPES? Given the difficulty in distinguishing Eu and CdAs terminated surfaces in $EuCd_2As_2$[13], interpretation of data obtained from surface sensitive techniques such as ARPES becomes ambiguous. In this article, we report investigations of the surface electronic structures of $EuZn_2As_2$ single crystals with STM/S and first-principles calculations. The surfaces were created by cleaving single crystals at liquid nitrogen temperature. Through STM/S, we find several types of surface and subsurface defects that have a profound impact on the surface electronic structure, thus allowing us to distinguish different terminations. There are distinct differences between the electronic structures of Eu- and ZnAs-terminated surfaces, which are elucidated by STS measurements. Our results allow us to address questions including (1) the surface atomic and electronic structures of $EuZn_2As_2$, (2) similarities and differences between Eu- and ZnAs-terminated surfaces, and (3) the impact of defects. Although the topological classifications of $EuZn_2As_2$ remain to be confirmed, the magnetic control of the surface state, whether topologically trivial or nontrival, is observed and explained. The electronic structure of $EuZn_2As_2$ is highly sensitive to both static magnetic ordering and magnetic fluctuation.

Results and discussion

Influence of heterogeneities on the surface electronic structures of $EuZn_2As_2$

$EuZn_2As_2$ crystallizes in a trigonal structure with the space group P-*3m1* (No. 164) with lattice constants of $a = b = 0.42$ nm, and $c = 0.72$ nm[16]. Figure 1a shows the ball and stick model of $EuZn_2As_2$ in the *bc* plane, showing that the AsZn slab is separated by Eu along the *c* direction. When a crystal is cleaved, the bonds between Eu (magenta) and As (green) atoms are expected to break, at the positions indicated by the two blue dashed lines in Fig. 1a. This is because the Eu-As bonding (with a bond length of 0.31 nm) is weaker compared to the As-Zn bonding (with a bond length of 0.25 nm)[16]. With two possible terminations shown in Fig. 1b, Eu or AsZn, step heights of 0.72 nm, or 0.48 nm, or their multiples could be observed. If only one termination were present, the step height is expected to be 0.72 nm or its multiples. Figure 1c presents an STM image of $EuZn_2As_2$ after an in-situ cleavage at 77 K. By scanning along the black line, we obtain the line profile as shown in Fig. 1c. It is obvious that multiple terraces with different step heights are present. Identifying the terminations of these terraces is a nontrivial task, as both the AsZn and Eu terminations have the same lattice constant, and symmetry as illustrated in Fig. 1b. Figures 1d and e show the STM images with atomic resolution. Through the presence of the unique defects combined with DFT calculations for the AsZn and Eu terminations, we identify that Fig. 1d is the AsZn surface while Fig. 1e is the Eu surface, with details described below.

As can be seen from Fig. 1d and e, there are defects at the cleaved surfaces, such as steps generated during cleavage, surface imperfections including absorbates, substitute atoms, vacancies, and scan-induced damage. Figure 1f shows a large-scale surface morphology of $EuZn_2As_2$ with atomic resolution, where defects are clearly seen. Figure 1g is the STS map collected simultaneously with the STM image shown in Fig. 1f. Note that atomic-level defects can drastically alter the surrounding electronic structure as indicated in blue "clouds" in the STS image with an affecting area of nearly 10 nm × 10 nm. To better illustrate the defects-induced surface electronic property changes, a much larger area of STM and STS images of $EuZn_2As_2$ are shown in Fig. 1h and i, respectively. From these images, multiple step heights are clearly seen, reflecting the presence of both terminations. Note that blue contrast extends beyond step edges, spreading into terraces and appears around defects (on the right large terrace). In brief, the influence of imperfections on the surface overwhelms the electronic properties over a much larger area than the physical extent of the defects. As such, it is difficult to distinguish the two possible surface terminations using conventional STM and STS imaging techniques.

Termination identification using substitutional defects

It is observed that a special group of substitutional defects can be used to differentiate the terminations because of their exclusivity on terminations, although the ascription of the terminations still cannot be identified only with the experimental data. Different from other structural defects like step edges or surface adsorbates, this group of equilateral-triangular-shaped defects, shows a modification to the local density of empty states around the defect (Figs. 2 and 3). Using the morphology and spectroscopy observations of the substitutional defects as inputs, deep kernel learning (DKL)

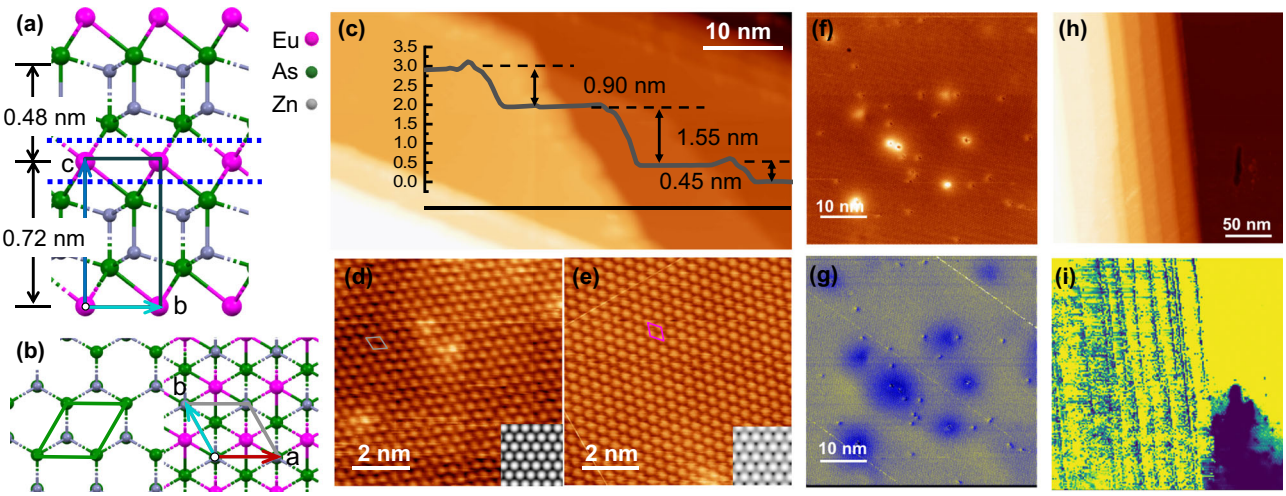

Fig. 1 | Crystal structure and morphology of $EuZn_2As_2$. **a** Sideview of the $EuZn_2As_2$ crystal structure. Two blue dashed lines represent possible terminations: Eu (magenta balls) and AsZn (green and grey balls). The black rectangle represents the unit cell in the ***b*** and ***c*** directions. **b** Top view of the AsZn and Eu terminations. The *ab*-plane unit cells are represented with solid green and gray parallelograms. **c** A large-scale STM topography of $EuZn_2As_2$ showing multiple steps and terraces with various step heights ($V_{bias} = -1.5$ V, $I_t = 50$ pA). The line profile along the black line is shown as an overlay. **d**, **e** STM images of the AsZn (**d**) and Eu (**e**) terminations with marked unit cells. $V_{bias} = -1.5$ V, $I_t = 20$ and 70 pA, respectively. Their simulated STM are presented as insets. **f** A typical high-resolution STM topography of the AsZn surface ($V_{bias} = -1.5$ V, $I_t = 50$ pA) with defects. **g** STS map collected simultaneously with (**f**). **h** An STM topography of $EuZn_2As_2$ with steps and terraces. **i** Integrated empty states image between 0 V and 1.5 V collected within the same area as (**h**).

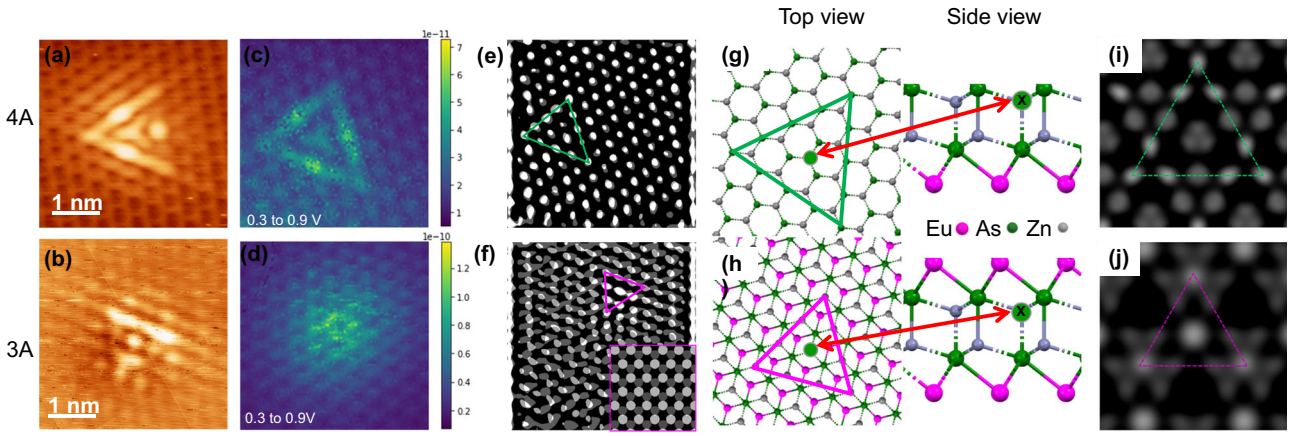

Fig. 2 | STM images, electronic properties, and structure models of the substitutional defects. STM images of (**a**) 4 A and (**b**) 3 A defects (set point: $V_{bias} = -1.5$ V, $I_t = 50$ pA). **c**, **d** Normalized integrated empty states from 0.3 V to 0.9 V of the 4 A and 3 A defects, respectively. Note the scale difference in the two-color bars. **e**, **f** Comparison of the superimpositions of two STS slices at 1.5 V and 1.075 V (50% transparency) from CITS maps, for 4 A and 3 A defects, respectively. The superposition of simulated STM images at 2 V and 1 V (65% transparency) of Eu termination is shown as an inset in (**f**). **g**, **h** Top and side view of the structure model of the 4 A and 3 A defects, outlined with green or magenta triangles with a green As atom in the middle. Red arrows point to the positions of the defected atoms (atoms with cross from the side view). **i**, **j** Simulated STM images for the corresponding 4 A and 3 A defects at 1 V, respectively.

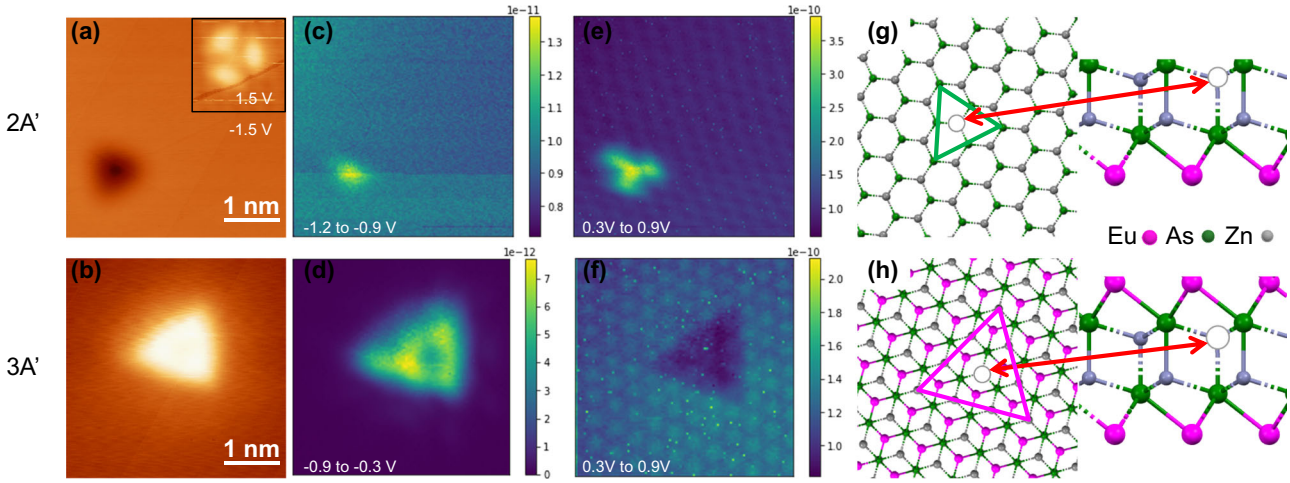

Fig. 3 | STM images, electronic properties, and structure models of vacancy defects. a, **b** STM images of (**a**) 2 A' and (**b**) 3 A' defects, set point: $V_{bias} = -1.5$ V, $I_t = 50$ pA. The inset of (**a**) shows a threefold symmetry petal of the 2 A' defect at $V_{bias} = 1.5$ V, $I_t = 50$ pA. **c**, **d** Integrated occupied state maps from −1.2 V to −0.9 V for 2 A' and from −0.9 V to −0.3 V for 3 A' defects, respectively. **e**, **f** Integrated empty state maps from 0.9 V to 0.3 V for 2 A' and 3 A' defects, respectively. **g**, **h** Top and side view of the structure models of the vacancy defects, outlined with green or magenta triangles with a missing Zn atom in the middle. Red arrows point to the positions of the defect location (white hollowed atom).

software[18,19] was used to survey the surface to establish statistics on the correlations between the defects and the local surface termination (i.e., particular kind of terrace). This DKL method enables much faster acquisition of structure-property correlations compared to the traditional operator-driven modes. The coexistence of 3 A defects (equilateral-triangular-shaped defects with three-atomic lengths) and 4 A defects (equilateral-triangular-shaped defects with four-atomic lengths) on the same surface termination was never observed. However, a coexistence of 3 A and 3 A' defects (see below and Fig. 3) was observed on the same terrace, and 4 A and 2 A' defects (see below and Fig. 3) were observed exclusively on the other kind of terrace.

Figure 2a and b present STM images with 4 A and 3 A defects, respectively. In addition to their size differences, the sides of the 3 A triangle are brighter at the corners while the sides of the 4 A triangle feature a bright spot at their center. The 4 A defect has a three-pointed star shaped weight center, while the weight center of 3 A is a single bright point. The apparent heights of the 4 A and 3 A defects in the STM images are in the range between 5 and 20 pm, which is too small to be surface adsorbates. For the substitutional defects, the dI/dV maps are integrated over the bias range that shows visible contrast. The data is further normalized by the energy range from 0.3 V to 0.9 V and are shown in Fig. 2c and d for the 4 A and 3 A defects, respectively. The triangle shape for 4 A remains unchanged through most of the energy slices (Fig. 2c), while the relative brightness of the 3 A defect shifts at different energies resulting in the fuzzy integrated map (Fig. 2d).

Shown in Fig. 2e and f are the superimpositions of the STS slices from continuous imaging tunneling spectroscopy (CITS) maps at 1.5 V and 1.075 V (50% transparency) of the surfaces with 4 A and 3 A defects, respectively. Apparently, the STS maps indicate different bias dependence between 4 A and 3 A contained surfaces. As outlined with green (Fig. 2e) and magenta (Fig. 2f) triangles, the atoms for the two energy slices overlay on top of each other in the whole areas for the surface containing 4 A defects. On the contrary, the atoms outside the triangle surprisingly shift at the two energies for the surface containing 3 A

defects, although the atoms within the magenta triangle overlay each other. This implies that, for the surface surrounding the 3 A defects, the visible atoms in STS switch from one element to another between the bias of 1.5 V to 1.075 V, while those within the 3 A defect area (magenta triangle) remain unchanged.

To understand the correlations between the defects and terminations, density functional theory (DFT) calculations are performed to sort out the observed distinct features of 4 A and 3 A defects. The simulated STM images of two pristine $EuZn_2As_2$ surfaces at −1.5 V are shown in the insets of Fig. 1d and e, respectively. Although they look similar, the visible atoms on the AsZn termination are As atoms, while on the Eu termination, they are Zn atoms. Within the experimental bias range, the brightest contrast is always from the As atom for the AsZn termination. But for the Eu termination, the brightest contrast alters from Zn (< 0.5 V) to As (0.5 V – 1.5 V) to Eu (> 1.5 V). The density of states (DOS) switching between 1 V to 2 V is presented in the superimpositions of the two images shown in the inset of Fig. 2f, where the bright atoms alternate from As (1 V) to Eu (2 V). Combining the experimental observations and DFT calculations, we identify the surface with 4 A defects as the AsZn termination and the one with 3 A defects as the Eu termination. Being able to identify surfaces is the key towards the study of the surface-state properties of topological materials.

A structure model with a substitutional atomic defect is proposed based on the STM/S signatures on 4 A and 3 A defects. The model proposes that the observed 4 A and 3 A defects have the same origin (i.e., an As atom substituting for Zn site), and the 4 A and 3 A signatures are from the projection of the same substitutional defect on the AsZn and Eu terminations, respectively. The size of the observed triangles is different due to the depth difference of the substitutional atom with respect to the surface. The crossed green atom in the center of the triangle in Fig. 2g, h is where the substitutional atom is located (Zn site), the side view shows the depth of the substitution (relative to the surfaces). The follow-up question is what atom occupies the Zn site? In $EuZn_2As_2$, As acts as an electron acceptor and it is unfavorable for either Eu or Zn to replace As. A more feasible scenario is that As is being misplaced and ultimately acting as an electron donor as well. Considering the radius differences among Eu^{2+} (1.25 Å), As^{3+} (0.7 Å), and Zn^{2+} (0.7 Å), it is likely that As^{3+} can be kinetically misplaced into a Zn^{2+} site such that As functions as an electron donor. This scenario is checked through DFT calculations. The simulated STM images based on the DFT calculations of the corresponding defects are shown in Figs. 2i and 2j, respectively. Note that the simulated STM images reproduce the main features of the experimental results. DFT based simulations of STM images were also carried out for other substitutional possibilities, none of which resembled the experimental images.

We conducted similar experimental and DFT studies on the surface vacancies. Shown in Fig. 3 are two types of vacancy defects marked as 2 A' and 3 A', respectively. The 2 A'-type vacancy is on the AsZn surface while the 3 A'-type vacancy is on the Eu surface based on our assignments above, and the finding of 2 A' defects only on the AsZn surface termination with 4 A defects, and the finding of 3 A' defects only on the Eu surface termination with 3 A defects. The line profile across the 2 A'-type vacancy gives a height decrease of ~70 pm, indicating a missing atom rather than a substitution. The image of 2 A'-type vacancy is bias dependent: it shows a threefold symmetry petal at 1.5 V (see the insert of Fig. 3a) but a void at −1.5 V (see Fig. 3a). On the other hand, the 3 A'-type vacancy changes from a bright triangle with a hollow center under negative bias (see Fig. 3b and d) to a uniform dark triangle when turning to a positive bias (Fig. 3f). Structural models of 2 A' defects on the AsZn termination and 3 A' defects on the Eu termination are presented in Fig. 3g and h, respectively. Similar to the 4 A and 3 A defects, the 2 A' and 3 A'defects have same origin (Zn vacancy), and they are the projection of the Zn vacancy defect on the As-Zn and Eu terminations, respectively.

Electronic properties of the defects and two terminations of $EuZn_2As_2$

According to first-principles calculations, bulk $EuZn_2As_2$ is expected to be semiconducting with a small bandgap[20]. Having identified the surfaces, we can now probe the surface conductance in each case. Figure 4a displays the averaged dI/dV spectra collected from CITS at two pristine surfaces as well as defected areas on a linear scale. For easy comparison, we also replot the data on a log scale in Fig. 4b. Both the pristine Eu and AsZn surfaces reveal zero conductance between −1 V and +0.5 V in the conductance band. This clearly indicates that the pristine surfaces of $EuZn_2As_2$ are insulating with ~1.5 V bandgap. While structural defects on the surface extend the gap in the conductance band to above 0.6 V (yellow curve in Fig. 4b), the substitutional (3 A and 4 A) and vacancy (2 A' and 3 A') defects presented above considerably reduce the bandgap width. Especially, on the AsZn surface, the conductance band edge is lowered by the substitutional and vacancy defects 4 A and 2 A' to around 0.3 V (0.29 V for 2 A', and 0.32 V for 4 A), while the valence band edge remains unchanged. On the Eu surface, both the 3A- and 3 A'-type defects drastically change the band gap widths through both valence and conductance band edges. For 3 A (the red curve in Fig. 4a–c), the band gap is 0.9 V, with band edges as – 0.65 V and +0.28 V; for 3 A' (the black curve in Fig. 4a–c), the band gap is 0.4 V, with band edges as – 0.34 V and +0.05 V.

The bandgap width decreases by the presence of 4 A and 3 A defects are also shown in the quasiparticle interference (QPI) maps acquired from the fast Fourier transformation (FFT) of STS maps. The QPI analysis is conducted in the energy range between −1.5 V and +1.5 V, with the 25 mV energy intervals. The momentum maps are shown in Fig. 4e and g, with the QPI map obtained from the STS map at 0.6 V shown in the insets, respectively. The red dashed lines mark the valence and conductance band edges of the pristine surfaces. The penetration of the states into the gap is clearly shown in Fig. 4f and h for defected surfaces. The reciprocal lattice points of the atomic lattice are observable at $q_x \approx 17.4\ nm^{-1}$, which is consistent with the atomic resolution STM images. QPI maps show a similar dispersing signal at $\bar{\Gamma}$ for all cases, but an additional QPI signal at $q \approx 8.7\ nm^{-1}$ along the $\bar{\Gamma}$-$\bar{K}$ direction is found for the surface containing 4 A defects, which corresponds to a new state inside the Brillouin zone. It occurs in the energy range of 0.5 ~ 1.5 eV as shown in Fig. 4f, marked by white arrows, from the interference of scattered quasiparticles. This indicates that the surface-projected electronic structure strongly depends on the specific defects. We consider that defects affect the scattering potentials that influence the relative intensity between the scattering wavevectors, which even modify the surface band structure with new scattering wavevectors.

It is apparent that the decrease of the bandgap by substitutional and vacancy defects is in the compensation of the DOS away from the Fermi level. The LDOS, calculated from $(dI/dV)/(I/V)$ in Fig. 4c, shows the comparison of the DOS changes of various cases. The two pristine terminations show the highest filled state peak (AsZn, green, −1.1 V) and the highest empty state peak (Eu, magenta, +1.2 V). This trend is consistent with the DFT calculated projected density of state (PDOS) shown in Fig. 4d. The presence of the defects suppresses those peaks and pushes more states into the bandgap, forming in-gap states.

According to experimental investigations, $EuCd_2As_2$ shows semimetallic behavior when the hole concentration is high[3,5] but is semiconducting when the hole concentration is low[10–13]. Bulk $EuZn_2As_2$ is also hole dominant[16] with nontrivial topological bands[21]. If the $EuZn_2As_2$ pristine surfaces preserve the same properties as that in the bulk, one expects that Zn vacancies introduce additional holes into the system. For As substitution into Zn sites, the situation is less clear. From the chemistry point of view (both ionic size and Zn function), As in the Zn site should behave as As^{3+}. The replacement of Zn^{2+} by As^{3+} will introduce an extra electron, thus reducing the overall hole concentration. Surprisingly, both substitutional and vacancy defects reduce the bandgap size regardless of the nature of the

defects-induced carriers. The defects-induced bandgap modification is much more dramatic on the Eu surface than that on the AsZn surface: (1) the bandgap in the area around the Zn vacancy on the Eu surface is 0.4 V but 1.3 V on the AsZn surface, and (2) the gap measured in the As substituted area is 0.9 V on the Eu surface but 1.3 V on the AsZn surface. This implies that the Eu layer plays an extremely important role in the electronic properties of $EuZn_2As_2$.

According to ref. 3, nontrivial topological bands were obtained by ARPES in the temperature window between 11 K and 17 K, which is just above T_N of $EuCd_2As_2$. The band splitting results from strong spin fluctuation, thus regarded as the Weyl state[3,4]. However, between 11 K and 17 K, the resistivity shows clearly non-metallic behavior[3,4], which makes one consider that the Weyl cone observed in ARPES reflects the surface state of $EuCd_2As_2$. For $EuZn_2As_2$, our experimental data in Fig. 4 shows no sign of the topological electronic structure at 77 K. Given that the resistivity decreases with decreasing temperature below T_N (~19 K)[16,17], we expect that the surface gap size decreases as well with decreasing temperature. Shown in Fig. 5 is the comparison of the averaged dI/dV and LDOS of the $EuZn_2As_2$ surface at 13 K, 16 K, and 19 K. The variable temperature STS data shows that the energy gap at the surfaces is closed when the sample is cooled down to below T_N with no gap observed at 13 K. Whether this gapless state is topologically nontrivial remains under further experimental investigation.

Furthermore, based on the quantitative analysis of defects effects to the LDOS, the gap size is greatly reduced with the defects in the Eu layer (3 A and 3 A') than that in the AsZn layer (4 A and 2 A') (see Fig. 4b). Within the Eu layer, the vacancy (3 A') results in a much smaller gap size than the As defect (3 A). This confirms the strong interplay between electronic properties and magnetism even at 77 K and the vacancy makes much greater suppression of local magnetic interaction than the As defect. The fact that defects in the Eu-terminated layer alter both valence and conduction bands further indicates the important contribution of local magnetism to LDOS, compared with the defects in the AsZn terminated layer which only lower down the density of the conduction states.

Combining the variable temperature LDOS in Fig. 5 and the understanding of defects' effects on two different surfaces, we can now reconcile the discrepancy between the LDOS distribution for both the pristine AsZn and Eu surfaces and the calculated PDOS shown in Fig. 4d. Our calculations were based on the A-type antiferromagnetically ordered state at 0 K for a slab with a clean and non-reconstructed surface. In our structural model, the unsaturated dangling bonds from a sharp cut of the surface tend to give in-gap surface states, yielding a conductive surface from calculations. Normally, calculated results can be used to compare with experimentally obtained results at finite temperatures such as electronic structure, defects effects, and structural parameters. The gap closing below T_N suggests that spin fluctuation above 19 K is responsible for the nonzero gap observed on the surface of the $EuZn_2As_2$. The discrepancies between the theoretical calculations (0 K) and the 77 K experimental results come from the dynamic spin fluctuation in the material, which unfortunately cannot be incorporated into simulation with our current DFT capability. Materials with strong spin-orbit coupling, magnetic frustration, or topological protection can exhibit surface gaps driven by magnetism, as seen in Kagome metals and other topological materials, where surface magnetism significantly modifies electronic structures as seen in $EuCd_2As_2$. Other examples include Mn-based Kagome metals like $TbMn_6Sn_6$[22] which exhibits a large Chern gap due to spin-orbit coupling and out-of-plane magnetization. Similar effects occur in topological materials such as Sb doped $MnBi_2Te_4$[23], where dopants can lead to the gapped topological

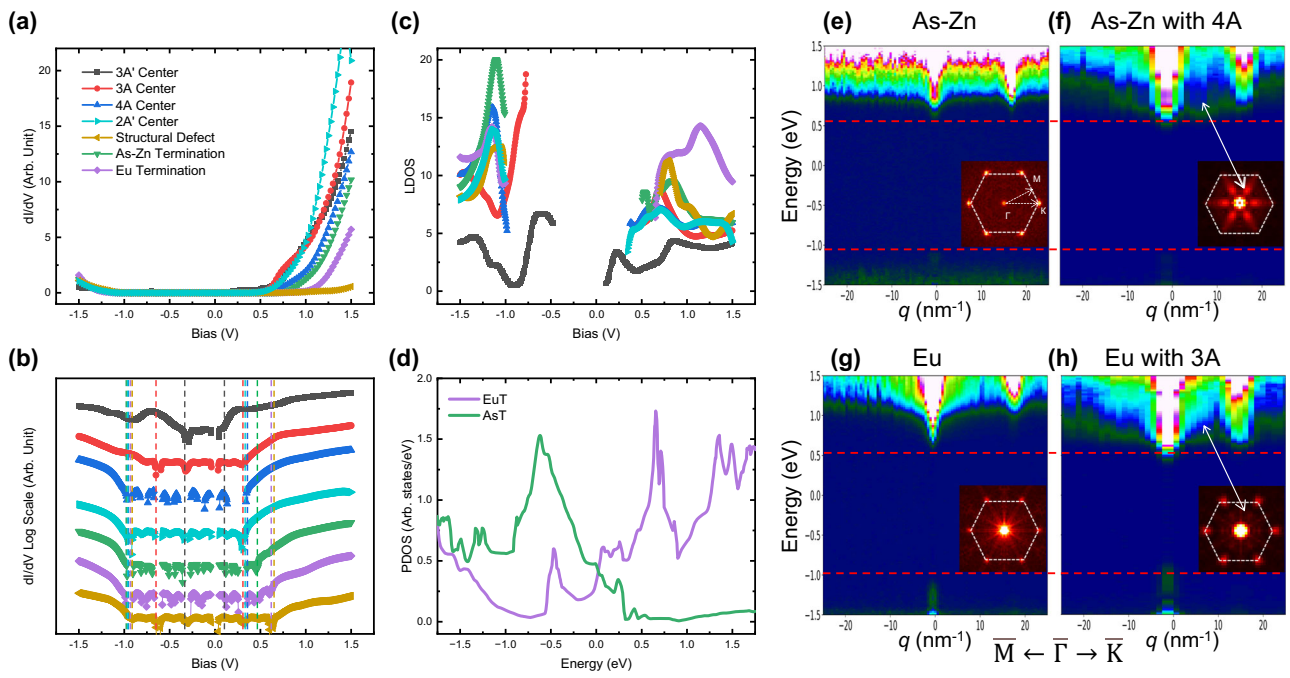

Fig. 4 | Influence of heterogeneities on the surface electronic structures and quasiparticle interference (QPI) comparison of the two terminations and defects. **a** Averaged STS spectra comparison of the two pristine surfaces, the two substitutional defects (3 A and 4 A), two vacancy defects (2 A' and 3 A'), and an area with structural defects. CITS set point: $V_{bias} = -1.5$ V, $I_t = 200$ pA. **b** STS spectra in (**a**) represented on a semi-log scale. Note the bandgap edges are marked by dashed lines. **c** Average local density of states (LDOS) derived from (**a**). **d** DFT calculated partial density of states (PDOS) of the two pristine terminations. **e**–**h** Energy vs. QPI signal in $\bar{M} - \bar{\Gamma} - \bar{K}$ directions for the pristine AsZn (**e**), AsZn and with 4 A defect (**f**), pristine Eu (**g**), Eu with 3 A (**h**) defects, respectively. QPI maps from the fast Fourier transformation (FFT) of the CITS are shown in the insets, energy at 1 V. The red dashed lines mark the valence and conductance band edges of the pristine surfaces. The white arrows points to the new states inside the Brillouin zone .

surface states. These findings highlight the critical role of surface magnetism in modifying electronic structures, particularly in materials with complex magnetic interactions. Given that spin fluctuation plays an important role above T_N of $EuZn_2As_2$ as discussed above, calculations that include spin fluctuation are needed.

Conclusions

We have investigated the surface electronic properties of $EuZn_2As_2$ using STM/S. The surfaces were created by cleaving $EuZn_2As_2$ single crystals at 77 K and studied at the same temperature. Two surfaces, Eu- and AsZn-terminated, with identical surface structures, were identified through defects-induced LDOS changes, which are confirmed by DFT simulations. The electronic structure of $EuZn_2As_2$ is highly sensitive to both static magnetic order and fluctuating magnetism. Several properties were observed: (1) both Eu and AsZn pristine surfaces are insulating with bandgap around 1.5 eV at 77 K, (2) the surface bandgap is dramatically reduced due to defects located in the Zn site, either Zn vacancy or As substitution, and (3) defects-induced LDOS changes are much more impactful on the Eu surface than on the AsZn surface, implying the importance of local magnetic interaction to the electronic properties. This is why our experimental results obtained at 77 K cannot be explained by DFT calculations for T = 0 K with an A-type antiferromagnetic ordering. Although the topological classifications of $EuZn_2As_2$ remain to be confirmed, our work sheds light on (1) the nature of the pristine surfaces of $EuZn_2As_2$ at 77 K, (2) defects effects on the surface electronic properties allowing us not only to identify the surfaces and the role of magnetic interaction in electronic properties, and (3) reconciliation of DFT simulations. Future work on the spin-polarized STM/S and DFT calculations incorporating magnetic fluctuation will help understand the role of magnetism and topology.

Methods

Crystal growth

Single crystals of $EuZn_2As_2$ were grown via the flux method using Sn with details described elsewhere[16]. The crystal structure was determined via x-ray diffraction at room temperature, which belongs to *P*-3*m*1 space group (#164) with the lattice constants $a = b = 0.421$ nm , and $c = 0.715$ nm. The magnetization measurements indicate the antiferromagnetic transition temperature $T_N = 19$ K. The in-plane electrical resistivity shows metallic behavior above ~ 200 K but nonmetallic below 200 K[16].

STM/S

The $EuZn_2As_2$ single crystals were cleaved on a cold stage which was cooled by liquid nitrogen under ultrahigh vacuum condition ($<1 \times 10^{-10}$ torr). The samples were immediately in situ transferred into a pre-cooled homemade high magnetic field low temperature scanning tunneling microscope. STM/STS experiments were carried out at 77 K and variable temperature from 5 K to 19 K with base pressure lower than 1×10^{-10} Torr using electrochemically etched Tungsten tips (W tip). All W tips were conditioned and checked using a clean Au (111) surface before each measurement. Topographic images were acquired in a constant current mode with a bias voltage applied to samples. All the spectroscopies were obtained using a lock-in amplifier with bias modulation $V_{rms} = 20$ mV at 977 Hz. Point spectroscopies, line spectroscopies, and CITS were collected at particular single point, along a defined line, and over a grid of pixels at bias ranges around Fermi level using the same lock-in amplifier parameters, respectively.

Machine learning method

The data analysis related to structure-property correlation was achieved using the deep kernel learning (DKL) framework. The DKL consists of a deep neural network (DNN) in combination with a Gaussian Process (GP) based regressor. The DNN consisted of three layers with the first, second, and third layers containing 64, 64, and 2 neurons respectively. The output of the last layer was treated as inputs to the GP regression. The inputs for the DKL were feature vectors extracted from the STM morphology image. This was trained against a suitable property scalar that was processed from the spectroscopic data. During the active learning process, the upper confidence bound acquisition function (UCB) was utilized to guide experimental exploration. In the UCB method, the β parameter was annealed in the range of 10 – 0.001, with a 10% reduction in every successive iteration. Open-source python packages Atomai (https://github.com/pycroscopy/atomai) was used for image processing and feature extraction, while Gpax (https://github.com/ziatdinovmax/gpax) was used for the DKL-based training and GP regression. These were integrated with LabVIEW programs to access the STM controls.

The integration of the dI/dV hyperspectral image from CITS was carried out in custom python 3.9.12 code. At each topological point, the dI/dV signals were integrated under the curve for all the bias slices within the bias range and then normalized. Then the matrix of the signal was utilized to

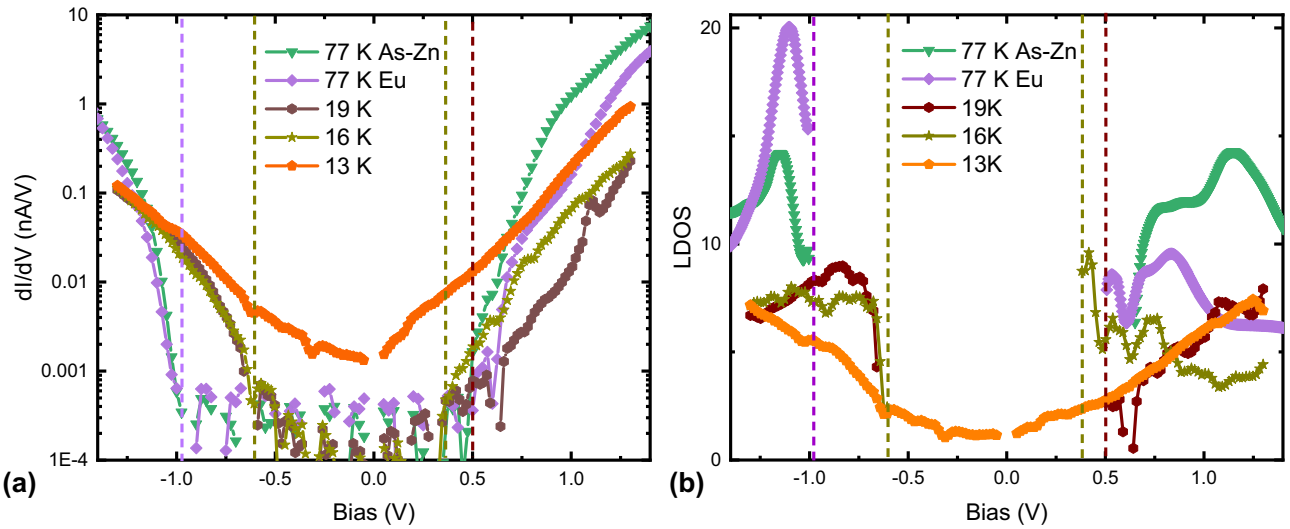

Fig. 5 | Comparison of the dI/dV and LDOS of the $EuZn_2As_2$ at different temperatures. Averaged STS spectra dI/dV on a semi-log scale (**a**) and LDOS (**b**) of the surfaces at 77 K, 19 K, 16 K and 13 K, respectively. The bandgap edges are marked by the dashed lines. STS set point: $V_{bias} = -1.5$ V, $I_t = 200$ pA for 77 K data, and −1.3 V and 200 pA for 13 K, 16 K and 19 K data. For direct comparison of all the dI/dV, they are normalized to the same set point of −1.3 V and 20 pA.

construct a pseudo-color image. The upper limits of the images were manually selected to maximize the number of features shown in the image.

Theoretical calculations

Density functional theory (DFT) calculations are performed using the projector augmented-wave (PAW) method as implemented in Vienna ab initio simulation package (VASP)[24,25]. The exchange correlation energy is described by the generalized gradient approximation (GGA) of Perdew-Burke-Ernzerhof (PBE) functional[26]. The valence configurations for each element are $5s^25p^66s^24f^7$ for Eu, $3d^{10}4s^2$ for Zn, and $4s^24p^3$ for As. To accurately describe the Coulomb correlations of the f orbitals, we use the spherically averaged DFT + U[27] with an on-site Coulomb interaction U of 6 eV. The cutoff of kinetic energy for plane wave expansion is set to 520 eV and the atoms are relaxed until the Hellmann-Feynman forces on each atom is below 0.01 eV/Å. We start from the five-atom primitive cell of bulk $EuZn_2As_2$ [as illustrated in Fig. 1a], and double the cell size by expanding the lattice parameter c by a factor of two, yielding a ten-atom unit cell for simulations. A Γ-centered **k**-point mesh of $7 \times 7 \times 2$ is used to sample the Brillouin zone of this unit cell. Lattice constants of $EuZn_2As_2$ unit cell are optimized to be $a = b = 0.425$ nm, and $2c = 1.447$ nm, in good agreement with the experimental values ($a = b = 0.42$ nm, and $c = 0.72$ nm).

The unit cell of $EuZn_2As_2$ contains two Eu atomic layers along the [001] direction, which are denoted as a "double layer" hereafter. The magnetic configuration considered in the calculations is type-A antiferromagnetic with interlayer spins aligned antiparallelly along the c axis and intralayer spins aligned parallelly. We study the (001) surface of $EuZn_2As_2$ and two surfaces can be distinguished: As- and Eu-terminated surfaces. By stacking *seven* unit cells of $EuZn_2As_2$ along the [001] direction, followed by removing the both top and bottom AsZn layers, and an inclusion of vacuum along [001] with a thickness of 15 Å, we create a slab with two Eu-terminated surfaces. By further removing the outer Eu layer from both the top and the bottom surface of the slab, while keeping the vacuum thickness the same, we create an As-terminated slab. To verify whether the slab is thick enough to prevent interactions between the two surfaces in the slab geometry, we look at the PDOS at each atomic layer plot. Additionally, we veri fied that PDOS at the surface will not change after adding more layers, confirming the validity of our slab model for surface calculations. We use the **k**-point grid of $7 \times 7 \times 1$ for all pristine surface calculations in the described slab geometry. To incorporate the substitutional surface defects in the slab and to reduce the impacts of the finite-size effect, we create a $3 \times 3 \times 1$ supercell for both terminations based on the previous slab geometry (576 atoms and 594 atoms for As- and Eu-terminated slabs, respectively) and introduce *one* defect on each surface of this $3 \times 3 \times 1$ supercell. The calculations for these larger supercells are performed using a single **k**-point at Γ. STM simulations are visualized using the p4vasp software package.

Data availability

The data sets that support the findings in this study are available from the corresponding author upon request.

Code availability

The codes that support the findings in this study are available from the corresponding author upon request.

Received: 23 August 2024; Accepted: 15 June 2025;
Published online: 10 July 2025

References

1. Bernevig, B. A., Felser, C. & Beidenkopf, H. Progress and prospects in magnetic topological materials. *Nature* **603**, 41–51 (2022).
2. Zhang, X. M. et al. Magnetic topological materials in two-dimensional: theory, material realization and application prospects. *Sci. Bull.* **68**, 2639–2657 (2023).
3. Ma, J. Z. et al. Spin fluctuation induced Weyl semimetal state in the paramagnetic phase of $EuCd_2As_2$. *Sci. Adv.* **5**, eaaw4718 (2019).
4. Jo, N. H. et al. Manipulating magnetism in the topological semimetal $EuCd_2As_2$. *Phys. Rev. B* **101**, 140402 (2020).
5. Taddei, K. M. et al. Single pair of Weyl nodes in the spin-canted structure of $EuCd_2As_2$. *Phys. Rev. B* **105**, L140401 (2022).
6. Riberolles, S. X. M. et al. Magnetic crystalline-symmetry-protected axion electrodynamics and field-tunable unpinned Dirac cones in $EuIn_2As_2$. *Nat. Commun.* **12**, 999 (2021).
7. Yan, J. et al. Field-induced topological Hall effect in antiferromagnetic axion insulator candidate $EuIn_2As_2$. *Phys. Rev. Res.* **4**, 013163 (2022).
8. Soh, J. R. et al. Ideal Weyl semimetal induced by magnetic exchange. *Phys. Rev. B* **100**, 201102 (2019).
9. Ma, J. et al. Emergence of nontrivial low-energy dirac fermions in antiferromagnetic $EuCd_2As_2$. *Adv. Mater.* **32**, 1907565 (2020).
10. Santos-Cottin, D. et al. $EuCd_2As_2$: a magnetic semiconductor. *Phys. Rev. Lett.* **131**, 186704 (2023).
11. Wang, Y. X. et al. Absence of metallicity and bias-dependent resistivity in low-carrier-density $EuCd_2As_2$. *Sci. China Phys. Mech.* **67**, 247311 (2024).
12. Nishihaya, S. et al. Intrinsic insulating transport characteristics in low-carrier density $EuCd_2As_2$ films. *Appl. Phys. Lett.* **124**, 023103 (2024).
13. Sun, Y. K. et al. Experimental evidence for field-induced metamagnetic transition of $EuCd_2As_2$. *J. Rare Earth* **40**, 1606–1610 (2022).
14. Gong, M. D. et al. Surface state evolution induced by magnetic order in axion insulator candidate $EuIn_2As_2$. *Phys. Rev. B* **106**, 125156 (2022).
15. Li, Y. et al. Surface and electronic structure of antiferromagnetic axion insulator candidate EuIn2As2. *Acta Phys. Sin.* **70**, 186801–186809 (2021).
16. Blawat, J. et al. Unusual electrical and magnetic properties in layered $EuZn_2As_2$. *Adv. Quantum Technol*. **5**, 2200012 (2022).
17. Regmi, P., Blawat, J. & Jin, R. Y. Large unconventional Hall effect observed in $EuZn_2As_2$. *Phys. Rev. B* **111**, 014422 (2025).
18. Liu, Y. et al. Experimental discovery of structure–property relationships in ferroelectric materials via active learning. *Nat. Mach. Intell.* **4**, 341–350 (2022).
19. Narasimha, G. et al. Uncovering multiscale structure-property correlations via active learning in scanning tunneling microscopy. *npj Comput. Mater.* **11**, 189 (2025).
20. Wang, Z. C. et al. Anisotropy of the magnetic and transport properties of $EuZn_2As_2$. *Phys. Rev. B* **105**, 165122 (2022).
21. Blawat, J., Speer, S., Singleton, J., Xie, W. W. & Jin, R. Y. Quantum-limit phenomena and band structure in the magnetic topological semimetal $EuZn_2As_2$. *Commun. Phys.* **6**, 255 (2023).
22. Yin, J. X. et al. Quantum-limit Chern topological magnetism in TbMnSn. *Nature* **583**, 533 (2020).
23. Ma, X. M. et al. Realization of a tunable surface Dirac gap in Sb-doped MnBiTe. *Phys. Rev. B* **103**, L121112 (2021).
24. Kresse, G. & Hafner, J. Ab-initio molecular-dynamics for open-shell transition-metals. *Phys. Rev. B* **48**, 13115–13118 (1993).
25. Kresse, G. & Furthmuller, J. Efficient iterative schemes for ab initio total-energy calculations using a plane-wave basis set. *Phys. Rev. B* **54**, 11169–11186 (1996).
26. Perdew, J. P., Burke, K. & Ernzerhof, M. Generalized gradient approximation made simple. *Phys. Rev. Lett.* **77**, 3865–3868 (1996).
27. Dudarev, S. L., Botton, G. A., Savrasov, S. Y., Humphreys, C. J. & Sutton, A. P. Electron-energy-loss spectra and the structural stability of nickel oxide: An LSDA + U study. *Phys. Rev. B* **57**, 1505–1509 (1998).

Acknowledgements

The STM work of this research was conducted at the Center for Nanophase Materials and Sciences, which is a DOE Office of Science User Facility. Work at USC (R.J.) was partially supported by the grant No. DE-SC0024501 funded by the U.S. Department of Energy, Office of Science. S.M. was supported by the startup fund from the USC and an ASPIRE grant from the

VPR's office of USC. This work used the Expanse supercomputer at the San Diego Supercomputer Center through allocation PHY230093 from the Advanced Cyberinfrastructure Coordination Ecosystem: Services & Support (ACCESS) program, which is supported by National Science Foundation Grants No. 2138259, No. 2138286, No. 2138307, No. 2137603, and No. 2138296. This research also used resources of the National Energy Research Scientific Computing Center (NERSC), a U.S. Department of Energy Office of Science User Facility operated under Contract No. DE-AC02-05CH11231.

Author contributions

D.K., G.N. and Z.G. conducted the STM/S studies and data analysis, D.K. and Z.G. conducted the QPI analysis; S.K. and S.M. conducted the DFT calculation, P.R. and R.J. grew the crystals; C.T., R.V. and I.H. involved in discussions; R.J. and Z.G. designed the experiments; all authors contributed to the writing of the manuscript.

Competing interests

The authors declare no competing interests.

Additional information

Supplementary information The online version contains supplementary material available at https://doi.org/10.1038/s42005-025-02190-2.

Correspondence and requests for materials should be addressed to Rongying Jin or Zheng Gai.

Peer review information *Communications Physics* thanks the anonymous reviewers for their contribution to the peer review of this work. A peer review file is available.